

# Observation of an exceptional nexus in ultracold atoms

Chenhao Wang,<sup>1, 2, \*</sup> Nan Li,<sup>1, 2, \*</sup> Jin Xie,<sup>1, 2</sup> Cong Ding,<sup>1, 2</sup> Zhonghua Ji,<sup>1, 2</sup> Liantuan Xiao,<sup>1, 2</sup> Suotang Jia,<sup>1, 2</sup> Ying Hu,<sup>1, 2, †</sup> Yanting Zhao<sup>1, 2, ‡</sup>

<sup>1</sup>State Key Laboratory of Quantum Optics and Quantum Optics Devices,  
Institute of Laser Spectroscopy, Shanxi University, Taiyuan 030006, China

<sup>2</sup>Collaborative Innovation Center of Extreme Optics, Shanxi University, Taiyuan 030006, China

In multistate non-Hermitian systems, higher-order exceptional points (EP) and exotic phenomena with no analogues in two-level systems arise, which have spawned intriguing prospects. A paradigm is an exceptional nexus (EX), a third-order EP as the cusp singularity of multiple exceptional arcs (EAs), that has a unique, hybrid topological nature. Using Bose-Einstein condensates to simulate the dynamics of a dissipative three-state system, we observe an EX formed by the coalescence of two EAs with different EP geometries. These exceptional structures are realized by controlling only two real parameters even in the absence of symmetry, and originate from the different roles of dissipation in the strong coupling limit and quantum Zeno regime, respectively. Our work paves the way for exploring higher-order EP physics in the many-body setting of ultracold atoms.

*Introduction*— The exceptional point (EP), a branch point singularity in the spectrum, is at the heart of many fascinating non-Hermitian phenomena and applications without Hermitian counterparts [1–4]. At an EP of order  $N$ ,  $N$  eigenvalues and the corresponding eigenstates of a non-Hermitian Hamiltonian simultaneously coalesce. The simplest is the second-order EP (EP2) of a two-state non-Hermitian Hamiltonian, which has been extensively studied in experiments [4]. Lately, observations of EP2s in quantum systems were reported, such as atoms [5–8], ion traps [9], single spins [10] and cavities [11].

In non-Hermitian systems with more than two states, multiple EPs can form and interact, resulting in qualitatively novel phenomenology absent in two-state cases [3, 4, 12–19]. Each trajectory of these EPs can trace out interesting geometries in the parameter space, yielding a kaleidoscope of arcs, rings, etc. Their interactions can lead to the coalescence of EPs and the creation of higher-order EPs, which further entail novel physics. A paradigm is where the coalescence of multiple exceptional arcs (EAs) consisting of EP2s produces an exceptional nexus (EX) [12, 15, 16], which is not only a third-order EP (EP3) but also a cusp singularity of EAs. Different from an EP2, which has a half topological charge, an EX has a hybrid topological nature associated with two distinct topological invariants [15, 16]. Thus, a system near the EX may exhibit peculiar, anisotropic nonanalytic responses to perturbations.

Nonetheless, the experimental explorations of higher-order EP related phenomena are generally difficult due to the requirement of tuning more parameters: An order- $N$  EP generically requires the tuning of  $2(N-1)$  real parameters in the absence of symmetry [17–20]. Initial experiments have been carried out in acoustics [12, 16, 21, 22], photonics [23, 24], electronic circuits [25] and photonic quantum walks [26]. Notably, observation of an EX in three-state acoustic systems with parity-time ( $\mathcal{PT}$ ) symmetry was reported [16]. However, higher-order EP physics has yet to be experimentally studied with ultracold atoms. In particular, an atomic realization of the

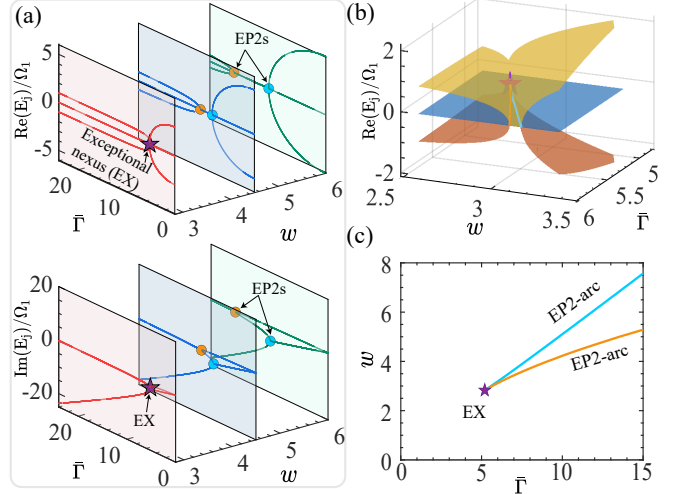


Figure 1. Exceptional arcs (EAs) with different EP geometries merge at the exceptional nexus (EX) in two-dimensional parameter space. (a) Calculated eigenvalues of Hamiltonian (1) as a function of dissipation rate  $\bar{\Gamma}$ , for coupling rate  $w = 6, 4.5, 2\sqrt{2}$  (green, blue, red), respectively. The real (imaginary) parts of eigenvalues are shown at the top (bottom). (b) Real parts of the eigenvalue Riemann surfaces. (c) Two EAs with different EP geometries merge at the EX in the  $(\bar{\Gamma}, w)$  plane. We use  $\Omega_1$  as the energy unit.

EX is highly desired, as it may lead to the possibility of exploring the interplay of EX and atomic interactions in the many-body setting of quantum gases.

In this work, we observe an EX formed by the coalescence of EAs based on Bose-Einstein condensates (BEC) of  $^{87}\text{Rb}$  atoms. By engineering coupled internal states of atoms, we realize a dissipative three-state model with a tunable dissipation rate. Through an extensive survey of the system dynamics under a wide range of parameters, we identify two EAs with different EP geometries: one arc is almost linear, while the other is roughly a parabola arc. We further demonstrate their coalescence produces an EX. The observations agree with the theory.

Our experiment has two distinct features relative to previous works: i) The EAs and EX are obtained by tun-

ing only two degrees of freedom despite the absence of  $\mathcal{PT}$  symmetry; ii) Appealingly, the two EAs exhibit different EP geometries. These intriguing EAs and EX result from the different roles of dissipation in the strong coupling limit and the quantum Zeno (QZ) limit [27], respectively. Our work thus complements existing experiments on three-state non-Hermitian Hamiltonians [4, 23, 26], which either require at least 3 degrees of freedom, or rely on non-Hermitian symmetry to alleviate the stringent parameter requirements, though this may entail identical geometries of potential EAs. We note that versatile EP geometries have recently attracted significant interest [4].

*Theoretical model* – We begin with theoretically describing the physics of a three-level system described by the non-Hermitian Hamiltonian (in the basis  $|1\rangle, |2\rangle, |3\rangle$ )

$$H = \Omega_1 \begin{pmatrix} 0 & 1 & 0 \\ 1 & 0 & w \\ 0 & w & -i\bar{\Gamma} \end{pmatrix}, \quad (1)$$

where the coherent coupling rate  $\Omega_1$  between states  $|1\rangle$  and  $|2\rangle$  is used as the energy unit. Hamiltonian  $H$  involves two degrees of freedom: the coherent coupling rate  $w \in \mathcal{R}$  between  $|2\rangle$  and  $|3\rangle$ , and the dissipation rate  $\bar{\Gamma} \in \mathcal{R}$  of  $|3\rangle$ . When  $\bar{\Gamma} = 0$ ,  $H$  reduces to the Hermitian one hosting a dark state, as familiar from quantum optics, quantum information, and quantum simulations.

For  $\bar{\Gamma} \neq 0$ , the non-Hermitian Hamiltonian (1) supports two EAs and an EX, despite the absence of non-Hermitian symmetries such as  $\mathcal{PT}$  symmetry. The intuitive picture can be obtained by analyzing the two opposite limits of  $H$  depending on  $\bar{\Gamma}/w$ :

i) In the strong-coupling limit  $w \gg 1$  (where the dissipation  $\bar{\Gamma} \lesssim w$  is relatively weak), state  $|2\rangle$  dominantly couples with  $|3\rangle$ , whereas  $|1\rangle$  is essentially decoupled at leading order. In the subspace spanned by  $|2\rangle$  and  $|3\rangle$ , thus, the effective two-level Hamiltonian takes the form  $H_{\text{eff}}/\Omega_1 = -i(\bar{\Gamma}/2)I + [w\sigma_x + i(\bar{\Gamma}/2)\sigma_z]$ , where  $I$  is the identity matrix and  $\sigma_i$  ( $i = x, y, z$ ) is the standard Pauli matrices. It describes a competition between the dissipation in  $|3\rangle$  and the coupling  $w$  that yields an EP2 at

$$w_{e_1} - \frac{1}{2}\bar{\Gamma}_{e_1} = 0. \quad (2)$$

For  $0 < \bar{\Gamma} < \bar{\Gamma}_{e_1}$ , the two eigenvalues of  $H_{\text{eff}}/\Omega_1$  have degenerate imaginary parts  $\bar{\Gamma}/2$ , which increases with  $\bar{\Gamma}$ , but the real parts  $\pm\sqrt{w^2 - \bar{\Gamma}^2/4}$  are non-degenerate and decrease with  $\bar{\Gamma}$ . For  $\bar{\Gamma} > \bar{\Gamma}_{e_1}$ , however, both eigenvalues  $i(-\bar{\Gamma}/2 \pm \sqrt{\bar{\Gamma}^2/4 - w^2})$  are purely imaginary and bifurcate. Thus, Equation (2) suggests an EP2-line in the  $(\bar{\Gamma}, w)$  plane; across this line, two eigenvalues of  $H$  changes their spectral properties, while the third eigenvalue stays  $\sim 0$ .

ii) In the opposite strong dissipation limit  $\bar{\Gamma} \gg w, 1$ , the QZ effect [27] can occur and confine the system in the subspace spanned by  $|1\rangle$  and  $|2\rangle$ , decoupled from  $|3\rangle$ . Adiabatically eliminating  $|3\rangle$ , the effective Hamiltonian in the Zeno-subspace is  $H'_{\text{eff}}/\Omega_1 = -i(w^2/2\bar{\Gamma})I + [\sigma_x +$

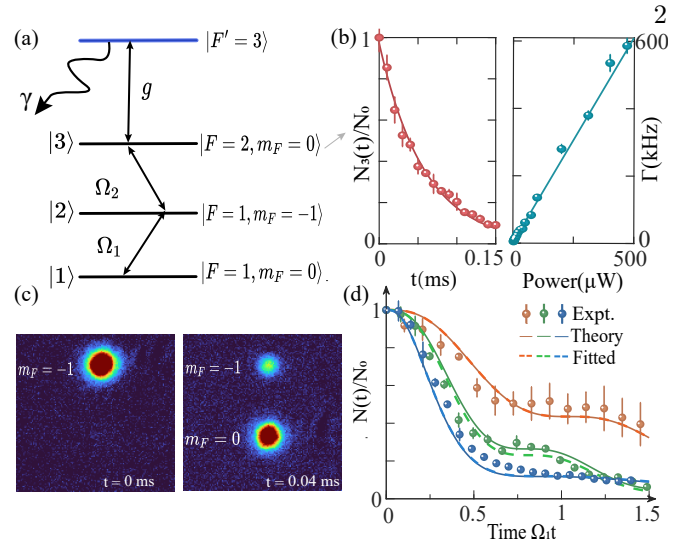


Figure 2. Experimental implementation with ultracold  $^{87}\text{Rb}$  atoms. (a) Energy level diagram. Three hyperfine states in the ground-state manifold,  $|F = 1, m_F = 0\rangle$ ,  $|F = 1, m_F = -1\rangle$  and  $|F = 2, m_F = 0\rangle$ , are used to encode  $|1\rangle$ ,  $|2\rangle$  and  $|3\rangle$ . A resonant radio-frequency field couples  $|F = 1, m_F = 0\rangle$  and  $|F = 1, m_F = -1\rangle$  with the coupling rate  $\Omega_1$ . A microwave field resonantly couples  $|F = 1, m_F = -1\rangle$  and  $|F = 2, m_F = 0\rangle$  with the coupling rate  $\Omega_2$ . A resonant laser drives a transition between  $|F = 2, m_F = 0\rangle$  and an electronically excited state  $|F' = 3\rangle$  with large spontaneous emission rate  $\gamma = 2\pi \times 6.06$  MHz (out of the system); the coupling rate  $g$  is laser tuned. Adiabatically eliminating  $|F' = 3\rangle$  leads to Eq. (1) with the dissipation rate  $\Gamma/\Omega_1 = \bar{\Gamma}$ . (b) Calibration and control of  $\Gamma$ . The data are the mean of five measurements. Left panel: Time-dependent atom population in  $|F = 2, m_F = 0\rangle$  is measured, by fitting (solid curve) which we extract  $\Gamma$  [28]. Right panel: the relation between measured  $\Gamma$  and the laser power is obtained by fitting [28]. (c) Stern-Gerlach absorption image of atom distributions in the two Zeeman levels ( $m_F = -1, 0$ ). The BEC is initialized in  $|F = 1, m_F = -1\rangle$ . After an evolution time  $t$ , the Stern-Gerlach absorption image is taken after 10 ms time of flight. Images are shown for  $t = 0$  and  $t = 0.04$  ms when  $\Omega_1 = 10.36$  kHz and  $\Omega_2 = 29.01$  kHz, corresponding to  $w = \Omega_2/\Omega_1 = 2.8$ . (d) Measured total atom number  $N(t)/N_0$  (normalized to the initial population  $N_0$ ) as a function of (dimensionless) time. The brown, green, and blue dots denote the data for renormalized parameters [28] ( $\bar{\Gamma} = 1, w = 2.8$ ), ( $\bar{\Gamma} = 2, w = 3.8$ ), ( $\bar{\Gamma} = 8, w = 4.5$ ), respectively. Each data is the average over 3 measurements. The error bars are the  $1\sigma$  standard deviation of measurements. The solid curves depict the numerical simulations with Eq. (1). The dashed curves denote the fitting [28].

$i(w^2/2\bar{\Gamma})\sigma_z]$ , where the effective decay rate in  $|2\rangle$  is suppressed by large  $\bar{\Gamma}$ . Thus an EP2 occurs at

$$\frac{1}{2}w_{e_2}^2 - \bar{\Gamma}_{e_2} = 0. \quad (3)$$

When  $\bar{\Gamma} < \bar{\Gamma}_{e_2}$ , the eigenvalues of  $H'_{\text{eff}}/\Omega_1$  are purely imaginary and bifurcate. However, when  $\bar{\Gamma} > \bar{\Gamma}_{e_2}$ , the eigen-decay rates coincide at  $\sim w^2/(2\bar{\Gamma})$  that decrease with  $\bar{\Gamma}$  due to Zeno effect, but the real parts bifurcate and asymptotically increase to  $\pm 1$  for  $\bar{\Gamma} \rightarrow \infty$ . Interestingly, Equation (3) implies a parabola EP2-arc quadratic

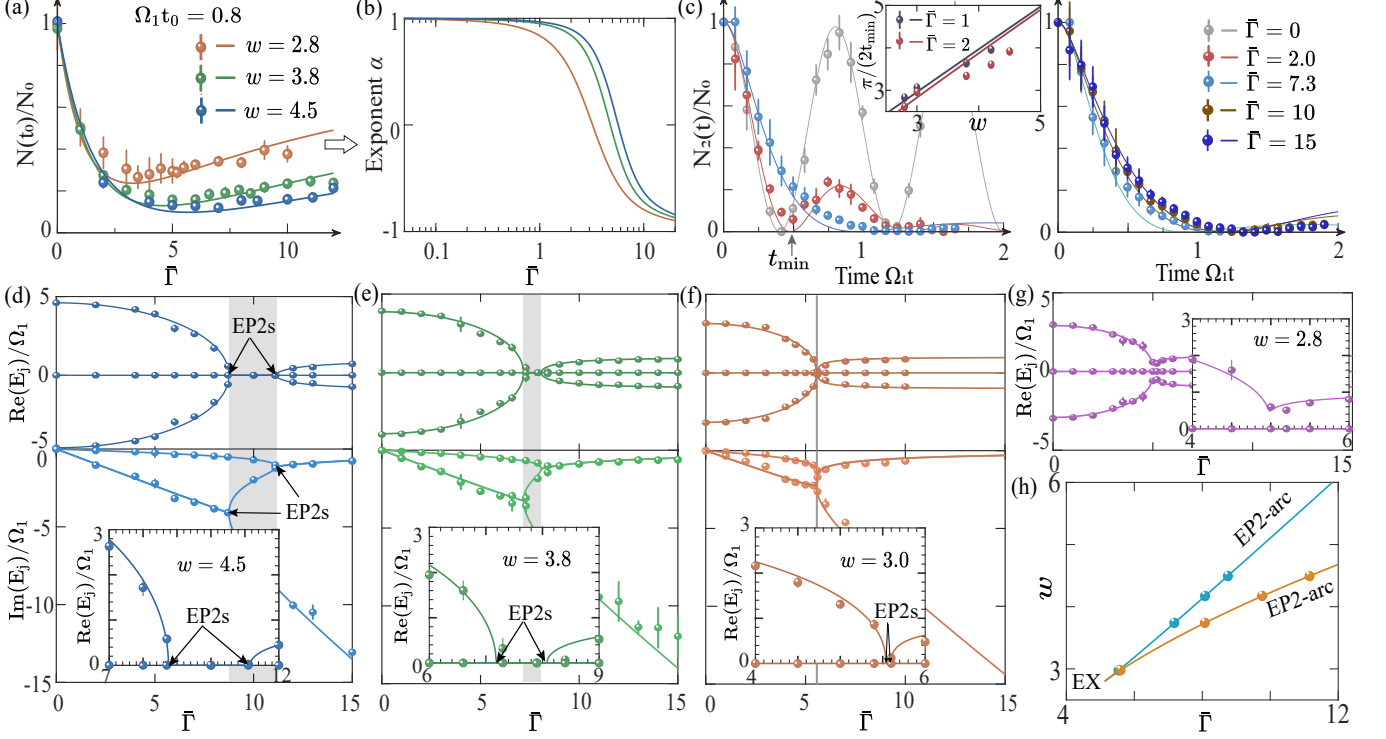


Figure 3. Observation of the EAs and EX that result from the different roles of dissipation in the strong coupling limit and quantum Zeno limit, respectively. (a) Measured total atom number  $N(t_0)/N_0$  at time  $\Omega_1 t_0 = 0.8$  as a function of the dissipation rate  $\bar{\Gamma}$ . The experimental data are shown for the coupling rate  $w = 2.8, 3.8, 4.5$  [28], respectively. Data within the time window  $\Omega_1 t_0 = 0.8 \pm 0.05$  are shown. The solid curves are the numerical fittings of the experimental data as a function of  $\bar{\Gamma}$ . (b) Exponent  $\alpha$  as a function of  $\bar{\Gamma}$ . Assuming the fitted  $N(t_0)/N_0$  in (a) is of the form  $N(t_0)/N_0 \simeq \exp(-\gamma t_0)$  with the scaling  $\gamma \propto \bar{\Gamma}^\alpha$ , we extract the exponent  $\alpha$  as a function of  $\bar{\Gamma}$ , for  $w = 2.8, 3.8, 4.5$  (brown, green, and blue), respectively. (c) Measured time evolution of the atom number  $N_2(t)/N_0$  in  $|F = 1, m_F = -1\rangle$ , for  $w = 3.8$ . Left panel:  $\bar{\Gamma}/w \lesssim 1$ . Right panel:  $\bar{\Gamma}/w \gtrsim 1$ . Solid curves are fitting. In the inset of the left panel, we extract the data of the (dimensionless) time  $t_{\min}$  when  $N_2(t)/N_0$  first reaches minimum, and plot  $\pi/(2t_{\min})$  as a function of  $w$  for  $\bar{\Gamma} = 1, 2$ . These data are compared with the estimated eigenfrequencies (solid curves) in the strong coupling limit (main text). (d)-(g) Measured eigenvalues as a function of  $\bar{\Gamma}$ , when (d)  $w = 4.5$ , (e)  $w = 3.8$ , (f)  $w = 3$  and (g)  $w = 2.8$ . In (d)-(f), both real (top) and imaginary (bottom) parts of the eigenvalues are shown. The gray shaded area indicates regions between the two EP2s. In (g), where  $w = 2.8 < w_{\text{EX}}$ , only the real part of eigenvalues is shown. The experimental data are obtained by fitting system parameters to the measured  $N(t)/N_0$  and then diagonalizing the fitted Hamiltonian. By further fitting (solid curves) the measured eigenvalues, we identify the degenerate points as the EPs. Insets of (d)-(f) are zoom-in plots of the measured eigenvalues near EPs. (h) Experimental EAs and EX in a two-dimensional parameter space  $(\bar{\Gamma}, w)$  shown on top of the theoretical results (solid curves). In (a) and (c), each data is the average over 3 measurements, and error bars denote  $1\sigma$  standard deviations. In (d)-(h), error bars denote the fitting errors.

in  $w$ , which is the different EP geometry from Eq. (2). When crossing this arc, two eigenvalues of  $H$  change their spectral properties in a way opposite to that in the limit i), while the third eigenvalue is  $\sim 0$ .

Thus, increasing  $\bar{\Gamma}/w$  in the Hamiltonian (1) from the weak dissipation limit  $\bar{\Gamma}/w \rightarrow 0$  to the strong dissipation limit  $\bar{\Gamma}/w \rightarrow \infty$  may result in two EP2s, and their coalescence creates an EX (EP3). This is numerically verified via exact solutions [28] of the eigenvalues  $E_j$  ( $j = 1, 2, 3$ ) of  $H$  various  $w$  and  $\bar{\Gamma}$  [Fig. 1(a)]. The merging of two EAs involving three states at an EX (EP3) is visualized on the eigenvalue Riemann surfaces [Fig. 1(b)], and more concisely in Fig. 1(c) in the  $(\bar{\Gamma}, w)$  plane. The EX occurs at  $w = 2\sqrt{2}$  and  $\bar{\Gamma} = 3\sqrt{3}$ , where all eigenvalues are degenerate at  $E_{\text{ep3}}/\Omega_1 = -i\sqrt{3}$ , and all eigenstates coalesce into  $|\psi\rangle_{\text{ep3}} = \frac{i}{\sqrt{6}}|1\rangle + \frac{1}{\sqrt{2}}|2\rangle - \frac{i}{\sqrt{3}}|3\rangle$ . The different EP geometries of the two arcs are also manifest in Fig. 1(c),

well approximated by Eqs. (2) and (3) [28].

*Experimental implementation* – Experimentally, we implement Eq. (1) based on the  $^{87}\text{Rb}$  BEC [Figs. 2(a) and (b)]. We exploit three ground-state hyperfine states ( $|F = 1, m_F = 0\rangle$ ,  $|F = 1, m_F = -1\rangle$  and  $|F = 2, m_F = 0\rangle$ ) of  $^{87}\text{Rb}$  atoms, respectively, to encode  $|1\rangle$ ,  $|2\rangle$  and  $|3\rangle$ ; we use an auxiliary electronically excited state  $|F' = 3\rangle$  with a large spontaneous emission rate  $\gamma = 2\pi \times 6.06$  MHz to engineer the dissipation rate  $\bar{\Gamma}$  in  $|3\rangle$ . A radio-frequency (RF) field is used to resonantly couple  $|F = 1, m_F = 0\rangle$  and  $|F = 1, m_F = -1\rangle$  with the coupling rate  $\Omega_1$ . A resonant microwave (MW) field couples  $|F = 1, m_F = -1\rangle$  and  $|F = 2, m_F = 0\rangle$  with the rate  $\Omega_2$ . We use a resonant laser to couple  $|F = 2, m_F = 0\rangle$  with the excited state  $|F' = 3\rangle$  with the coupling rate  $g$ . Since  $|F' = 3\rangle$  is barely populated due to the large  $\gamma$ , it can be adiabatically eliminated to yield  $\Gamma = g^2/\gamma$  in  $|F = 2, m_F = 0\rangle$ , i.e., whenever atoms

populate  $|F = 2, m_F = 0\rangle$ , they are lost from the system at the rate  $\Gamma$ . All relevant parameters can be flexibly controlled via lasers. In Fig. 2(c), we show the calibration of  $\Gamma$ . Finally, focusing on the probability of finding atoms remaining in the system, their time evolution is governed by the effective Hamiltonian  $H$  in Eq. (1) with  $w = \Omega_2/\Omega_1$  and  $\bar{\Gamma} = \Gamma/\Omega_1$ .

To confirm the implementation, in each measurement, we start with preparing a BEC with  $N_0 \sim 2.5 \times 10^4$   $^{87}\text{Rb}$  atoms in  $|F = 1, m_F = -1\rangle$  at the temperature  $\sim 50$  nK [c.f. left panel of Fig. 2(c)]. Then we sweep the bias magnetic field to 16 G within 100 ms and wait 100 ms for the bias field to stabilize. Afterward, we suddenly turn on the MW field, RF field, and the resonant laser to generate all the couplings [28]. This drives the time evolution of the BEC, when all three hyperfine states  $|F = 1, m_F = 0\rangle$ ,  $|F = 1, m_F = -1\rangle$  and  $|F = 2, m_F = 0\rangle$  are populated. After an evolution time  $t$ , we apply the Stern-Gerlach absorption imaging technique after a 10 ms time of flight [c.f. the right panel of Fig. 2(c)] and measure the atomic populations in the two Zeeman levels with  $m_F = 0, -1$ , respectively. In Fig. 2(d), the time evolution of the measured (normalized) total atom number  $N(t)/N_0$  are shown for various  $w$  and  $\bar{\Gamma}$  [28]. The experiment data agree well with the numerical simulations (solid curves) based on  $H$ .

*Observing the formation of EX by merging EAs* – We first probe the dynamical signatures associated with different interplays of dissipation and coherent processes that lead to different EAs, starting from the atom number loss. In Fig. 3(a), the measured  $N(t_0)/N_0$  at a fixed time  $\Omega_1 t_0 = 0.8 \pm 0.05$  is shown as a function of  $\bar{\Gamma}$  [28]. For  $\bar{\Gamma}/w < 1$ ,  $N(t_0)/N_0$  decreases with  $\bar{\Gamma}$ , indicating enhanced atomic loss; the curves for different coupling  $w$  significantly overlap, which signals that the underlying eigen-decay rates are insensitive to  $w$ . These features agree with the predictions in the strong coupling limit in i). When  $\bar{\Gamma}/w \gg 1$ , in contrast, we observe a revival of the population when  $\bar{\Gamma}$  increases, in such a way that depends on  $w$ , consistent with the analysis in QZ regime. We also see less atomic loss and faster revival for smaller  $w$ ; this is expected, as a BEC initialized in  $|F = 1, m_F = -1\rangle$  dissipates mainly through tunneling to  $|F = 2, m_F = 0\rangle$ . To further reveal how the atom behaves under different  $\bar{\Gamma}$ , we fit the measured  $N(t_0)/N_0$  as a function of  $\bar{\Gamma}$  (solid curve). Using the fitted curve and assuming  $N(t_0)/N_0 \simeq \exp(-\gamma t_0)$  with  $\gamma \propto \bar{\Gamma}^\alpha$ , we extract the exponent  $\alpha$  as a function of  $\bar{\Gamma}$  in Fig. 3(b). The  $\alpha$  of various  $w$  exhibits similar asymptotic behaviors, which always crossover from  $\alpha \simeq 1$  in the limit  $\bar{\Gamma}/w \rightarrow 0$  toward  $\alpha \rightarrow -1$  when  $\bar{\Gamma}/w \gg 1$ . These observations support the predictions on  $\text{Im}(E_j)$  in two opposite limits.

To probe the behaviors of  $\text{Re}(E_j)$ , we measure the time-dependent atom population  $N_2(t)/N_0$  in  $|F = 1, m_F = -1\rangle$  that encodes  $|2\rangle$ ; see Fig. 3(c) for  $w = 3.8$ . The left panel shows the case for  $\bar{\Gamma} \lesssim w$  corresponding to the limit i). Clear oscillation is observed, indicating the existence of non-degenerate  $\text{Re}(E_j)$ . To estimate  $\text{Re}(E_j)$ ,

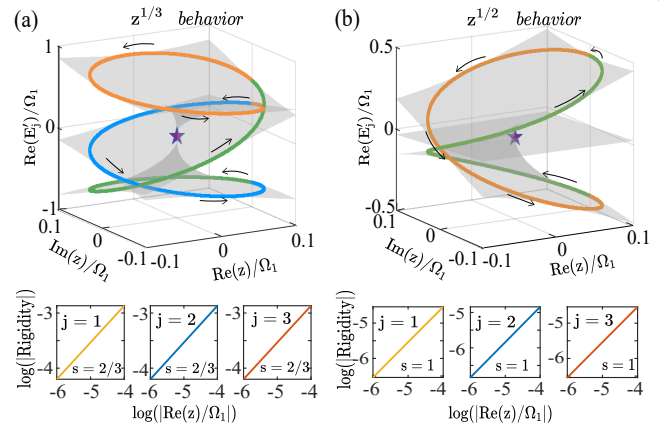


Figure 4. Illustrations of the anisotropic perturbation behaviors around the EX (purple star). (a)  $z^{1/3}$  perturbation behavior. (b)  $z^{1/2}$  perturbation behavior. We numerically calculate the eigenvalues  $E'_j$  ( $j = 1, 2, 3$ ) and eigenstates of the perturbed Hamiltonian  $H' = H + zH_1$ , with the complex perturbation parameter  $z/\Omega_1 = 0.1e^{i\theta}$  [ $\theta \in [0, 2\pi]$ ]. We use  $H_1 = |3\rangle\langle 3|$  in (a) and Eq. (4) for  $H_1$  in (b). Top panels: real parts of  $E'_j$  as a function of  $z$ . Bottom panels: variation of the phase rigidity [28] of each perturbed eigenstate with  $\text{Re}(z)$ , from which the critical exponent  $s$  is extracted.

we fit the measured  $N_2(t)/N_0$  and read off the time  $t_{\min}$  when  $N_2(t)/N_0$  first hits minimum. In the inset, we show the data of  $\pi/(2t_{\min})$  as a function of  $w$ . We see that the smaller  $\bar{\Gamma}/w$  is, there is better agreement with the asymptotic expression  $\text{Re}(E_j)/\Omega_1 = \sqrt{w^2 - \bar{\Gamma}^2}/4$  (solid curves) from previous analysis. When  $\bar{\Gamma} \gtrsim w$  [right panel of Fig. 3(c)] corresponds to the limit ii), a very slow oscillation seems to occur, but the observation of a full oscillation is not available on the time scales of our measurements.

To verify the formation of EX, which is not only an EP3 but also a cusp singularity of two EAs, we carefully retrieve eigenvalues of  $H$  by fitting the experimental  $N(t)/N_0$  [c.f. dashed curves in Fig. 2(d)] and diagonalizing the Hamiltonian with the fitted parameters [28]. The measured eigenvalues are shown in Figs. 3(d)-(g) as a function of  $\bar{\Gamma}$ , for  $w = 4.5, 3.8, 3, 2.8$ , respectively. There, we identify potential EP2s by fitting [28] the measured eigenvalues as a function of  $\bar{\Gamma}$ . In Fig. 3(d)-(f), we identify two EP2s whose separation shrinks when  $w$  decreases, i.e., the EP2s are merging. The two sufficiently close EP2s in Fig. 3(f) strongly evidence the existence of an EP3. To further verify the cusp singularity aspect of the degenerate point, we tune  $w$  immediately below EP3. As shown in Fig. 3(g), all three eigenvalues become non-degenerate, which signals the termination of EP2-arcs at EP3, i.e., to form a cusp singularity.

Finally, we construct the trajectories of EP2 in the  $(\bar{\Gamma}, w)$  plane in Fig. 3(h), where the experimental data are shown on top of the theoretical results. The good agreement between the experiment and theory evidences the EX formed by two EAs with different EP geometries.

*Discussion* – A feature of the system at an EX concerns the anisotropic nonanalytic response to perturbations

$H_1$  [14]. For the perturbed Hamiltonian  $H' = H + zH_1$  with the complex perturbation parameter  $z$  ( $|z|/\Omega_1 \rightarrow 0$ ), two possible behaviors emerge depending on  $H_1$  [28]: i) The leading correction  $\delta E'_j$  of three eigenvalues scales as  $\propto z^{1/3}$ ; ii)  $\delta E'_j$  of two eigenvalues scale as  $\propto z^{1/2}$ , while the remaining one obeys standard Taylor expansion. This is related to the hybrid topological nature of the EX, which can be revealed by the critical exponent  $s$  of the phase rigidity of the perturbed eigenstates [15, 16]:  $s = 2/3$  for i) and  $s = 1$  for ii). Figure 4 numerically illustrates the two kinds of behaviors around the EX of Eq. (1). In Fig. 4(a), we assume  $H_1 = |3\rangle\langle 3|$ , while in Fig. 4(b), we consider a non-Hermitian perturbation

$$H_1 = \begin{pmatrix} 0 & 0 & i \\ \frac{\sqrt{3}}{3} & 0 & \frac{\sqrt{6}}{6} \\ -i & 0 & 0 \end{pmatrix}. \quad (4)$$

In cold atoms, the former perturbation represents imperfections in the detuning and local dissipation, while the latter may result from the presence of both coherent and dissipative couplings [29]. As detailed in Supplementary Materials [28], we calculate the eigenvalues  $E'_j$  of  $H'$ , whose real parts are shown with respect to a cyclic path of  $z/\Omega_1 = 0.1e^{i\theta}$  (top panels); we also calculate the corresponding eigenstates and show the critical exponent  $s$

of the phase rigidity in bottom panels. In Fig. 4(a), we see typical  $z^{1/3}$  perturbation behavior, where three perturbed eigenvalues are the three branches of a third-root expansion, and the critical exponent of perturbed eigenstate is  $s = 2/3$ . In contrast, Figure 4(b) shows the  $z^{1/2}$  behavior, where two states are transversed in cyclic perturbations around the EX without affecting the third state at the leading order of  $z$ , corresponding to  $s = 1$ .

In summary, we observe an EX formed by the coalescence of EAs with different EP geometries based on ultracold atoms. Since the EAs stem from the different interplays of the coupling and dissipation in different regimes, the consequent EX can exist in 2D parameter space despite the absence of non-Hermitian symmetry, and is robust against imperfections provided this physical picture holds. While the atomic interaction is ignorable in the present setup, our work sets the stage for exploring the interplay of the EX and highly tunable interactions [30] of cold atoms, and the resulting peculiar perturbation responses of quantum gases.

*Acknowledgments* – This research is funded by the National Key Research and Development Program of China (No. 2022YFA1404201), and the National Natural Science Foundation of China (Grants No. 12274272, 12034012, 61827824, 12074231, 12374246).

\* These two authors contributed equally.

† huying@sxu.edu.cn

‡ zhaoyt@sxu.edu.cn

- [1] W. D. Heiss, The Physics of Exceptional Points, *J. Phys. A: Math. Theor.* **45**, 444016 (2012).
- [2] Y. Ashida, Z. Gong, and M. Ueda, Non-Hermitian Physics, *Adv. Phys.* **69**, 249 (2020).
- [3] E. J. Bergholtz, J. C. Budich, and F. K. Kunst, Exceptional Topology of Non-Hermitian Systems, *Rev. Mod. Phys.* **93**, 015005 (2021).
- [4] K. Ding, C. Fang, and G. Ma, Non-Hermitian Topology and Exceptional-Point Geometries, *Nat. Rev. Phys.* **4**, 745 (2022).
- [5] P. Peng, W. Cao, C. Shen, W. Qu, J. Wen, L. Jiang, and Y. Xiao, Anti-Parity-Time Symmetry with Flying Atoms, *Nat. Phys.* **12**, 1139 (2016).
- [6] J. Li, A. K. Harter, J. Liu, L. De Melo, Y. N. Joglekar, and L. Luo, Observation of Parity-Time Symmetry Breaking Transitions in a Dissipative Floquet System of Ultracold Atoms, *Nat. Commun.* **10**, 855 (2019).
- [7] Z. Ren, D. Liu, E. Zhao, C. He, K. K. Pak, J. Li, and G.-B. Jo, Chiral Control of Quantum States in Non-Hermitian Spin-Orbit-Coupled Fermions, *Nat. Phys.* **18**, 385 (2022).
- [8] C. Liang, Y. Tang, A.-N. Xu, and Y.-C. Liu, Observation of Exceptional Points in Thermal Atomic Ensembles, *Phys. Rev. Lett.* **130**, 263601 (2023).
- [9] L. Ding, K. Shi, Q. Zhang, D. Shen, X. Zhang, and W. Zhang, Experimental Determination of PT-Symmetric Exceptional Points in a Single Trapped Ion, *Phys. Rev. Lett.* **126**, 083604 (2021).
- [10] Y. Wu, W. Liu, J. Geng, X. Song, X. Ye, C.-K. Duan, X. Rong, and J. Du, Observation of Parity-Time Symmetry Breaking in a Single-Spin System, *Science* **364**, 878 (2019).
- [11] Y. Choi, S. Kang, S. Lim, W. Kim, J.-R. Kim, J.-H. Lee, and K. An, Quasieigenstate Coalescence in an Atom-Cavity Quantum Composite, *Phys. Rev. Lett.* **104**, 153601 (2010).
- [12] K. Ding, G. Ma, M. Xiao, Z. Q. Zhang, and C. T. Chan, Emergence, Coalescence, and Topological Properties of Multiple Exceptional Points and Their Experimental Realization, *Phys. Rev. X* **6**, 021007 (2016).
- [13] E. M. Graefe, U. Günther, H. J. Korsch, and A. E. Niederle, A Non-Hermitian  $\mathcal{PT}$  Symmetric Bose-Hubbard Model: Eigenvalue Rings from Unfolding Higher-Order Exceptional Points, *J. Phys. A: Math. Theor.* **41**, 255206 (2008).
- [14] G. Demange and E.-M. Graefe, Signatures of Three Coalescing Eigenfunctions, *J. Phys. A: Math. Theor.* **45**, 025303 (2012).
- [15] Y.-X. Xiao, Z.-Q. Zhang, Z. H. Hang, and C. T. Chan, Anisotropic Exceptional Points of Arbitrary Order, *Phys. Rev. B* **99**, 241403(R) (2019).
- [16] W. Tang, X. Jiang, K. Ding, Y.-X. Xiao, Z.-Q. Zhang, C. T. Chan, and G. Ma, Exceptional Nexus with a Hybrid Topological Invariant, *Science* **370**, 1077 (2020).
- [17] I. Mandal and E. J. Bergholtz, Symmetry and Higher-Order Exceptional Points, *Phys. Rev. Lett.* **127**, 186601 (2021).
- [18] P. Delplace, T. Yoshida, and Y. Hatsugai, Symmetry-Protected Multifold Exceptional Points and Their Topo-

logical Characterization, *Phys. Rev. Lett.* **127**, 186602 (2021).

[19] S. Sayyad and F. K. Kunst, Realizing Exceptional Points of Any Order in the Presence of Symmetry, *Phys. Rev. Res.* **4**, 023130 (2022).

[20] L. Pan, S. Chen, and X. Cui, High-Order Exceptional Points in Ultracold Bose Gases, *Phys. Rev. A* **99**, 011601 (R) (2019).

[21] X. Fang, N. J. R. K. Gerard, Z. Zhou, H. Ding, N. Wang, B. Jia, Y. Deng, X. Wang, Y. Jing, and Y. Li, Observation of Higher-Order Exceptional Points in a Non-Local Acoustic Metagrating, *Commun. Phys.* **4**, 271 (2021).

[22] W. Tang, K. Ding, and G. Ma, Experimental Realization of Non-Abelian Permutations in a Three-State Non-Hermitian System, *Natl. Sci. Rev.* **9**, nwac010 (2022).

[23] H. Hodaei, A. U. Hassan, S. Wittek, H. Garcia-Gracia, R. El-Ganainy, D. N. Christodoulides, and M. Khasavikhan, Enhanced Sensitivity at Higher-Order Exceptional Points, *Nature* **548**, 187 (2017).

[24] J. Del Pino, J. J. Slim, and E. Verhagen, Non-Hermitian Chiral Phononics through Optomechanically Induced Squeezing, *Nature* **606**, 82 (2022).

[25] J. Hu, R.-Y. Zhang, Y. Wang, X. Ouyang, Y. Zhu, H. Jia, and C. T. Chan, Non-Hermitian Swallowtail Catastrophe Revealing Transitions among Diverse Topological Singularities, *Nat. Phys.* **19**, 1098 (2023).

[26] K. Wang, L. Xiao, H. Lin, W. Yi, E. J. Bergholtz, and P. Xue, Experimental Simulation of Symmetry-Protected Higher-Order Exceptional Points with Single Photons, *Sci. Adv.* **9**, eadi0732 (2023).

[27] P. Facchi and S. Pascazio, Quantum Zeno Dynamics: Mathematical and Physical Aspects, *J. Phys. A: Math. Theor.* **41**, 493001 (2008).

[28] See details in Supplementary Materials, where we provide details on the exact solutions of eigenvalues, experimental details on the calibration and fitting, supplementary data on the dynamics, and detailed theory on the anisotropic perturbation behaviors around the EX (including anisotropic eigenvalues and hybrid topological property).

[29] W. Gou, T. Chen, D. Xie, T. Xiao, T.-S. Deng, B. Gadway, W. Yi, and B. Yan, Tunable Nonreciprocal Quantum Transport through a Dissipative Aharonov-Bohm Ring in Ultracold Atoms, *Phys. Rev. Lett.* **124**, 070402 (2020).

[30] Y. Wang, J.-H. Zhang, Y. Li, J. Wu, W. Liu, F. Mei, Y. Hu, L. Xiao, J. Ma, C. Chin, and S. Jia, Observation of Interaction-Induced Mobility Edge in an Atomic Aubry-André Wire, *Phys. Rev. Lett.* **129**, 103401 (2022).

# Supplementary Material for “Observation of an exceptional nexus in ultracold atoms”

Chenhao Wang,<sup>1, 2, \*</sup> Nan Li,<sup>1, 2, \*</sup> Jin Xie,<sup>1, 2</sup> Cong Ding,<sup>1, 2</sup> Zhonghua Ji,<sup>1, 2</sup> Liantuan Xiao,<sup>1, 2</sup> Suotang Jia,<sup>1, 2</sup> Ying Hu,<sup>1, 2, †</sup> Yanting Zhao<sup>1, 2, ‡</sup>

<sup>1</sup>State Key Laboratory of Quantum Optics and Quantum Optics Devices,  
Institute of Laser Spectroscopy, Shanxi University, Taiyuan 030006, China

<sup>2</sup>Collaborative Innovation Center of Extreme Optics, Shanxi University, Taiyuan 030006, China

## I. ANALYTICAL SOLUTIONS OF THE EIGENVALUES

Here we present the analytical solutions of the eigenvalues for the three-level non-Hermitian Hamiltonian in Eq. (1) of the main text. Mathematically, the three eigenvalues are the roots of the cubic equation

$$ax^3 + bx^2 + cx + d = 0. (a \neq 0) \quad (1)$$

The general condition for the existence of degenerate roots of Eq. (1) is that the discriminant equals zero, i.e.,

$$\Delta = B^2 - 4AC = 0, \quad (2)$$

where  $A = b^2 - 3ac$ ,  $B = bc - 9ad$ , and  $C = c^2 - 3bd$ .

For the considered Hamiltonian in the main text, we have the coefficients  $a = 1$ ,  $b = i\bar{\Gamma}$ ,  $c = -(1 + w^2)$ , and  $d = -i\bar{\Gamma}$ . The condition (2) with  $A \neq 0$  and  $B \neq 0$  leads to two curves (i.e., EAs) described by the equations

$$\begin{aligned} \bar{\Gamma}^2 &= \pm \frac{\sqrt{(w^4 + 20w^2 - 8)^2 - 64(w^2 + 1)^3}}{8} \\ &+ \frac{5w^2}{2} + \frac{w^4}{8} - 1. \end{aligned} \quad (3)$$

Note that, as shown in the supplementary Fig. 1, Equations (2) and (3) in the main text (dashed curves), respectively, provide good approximations in describing EAs (solid curves).

When  $A = B = 0$  in Eq. (2), corresponding to  $w = 2\sqrt{2}$  and  $\bar{\Gamma} = 3\sqrt{3}$  in our case, we obtain a triple-degenerate root  $x_1 = x_2 = x_3 = -\sqrt{3}i$ , i.e., the EP3. Substituting this into Eq. (1) in the main text, we straightforwardly obtain the corresponding eigenstate at EP3.

In general, the three solutions of Eq. (1) are given by

$$\begin{aligned} x_1 &= m + n - \frac{b}{3a}, \\ x_2 &= \omega m + \omega^2 n - \frac{b}{3a}, \\ x_3 &= \omega^2 m + \omega n - \frac{b}{3a}. \end{aligned}$$

Here  $\omega = -\frac{1}{2} + \frac{\sqrt{3}}{2}i$ ,  $m$ , and  $n$  are expressed as

$$\begin{aligned} m &= \sqrt[3]{u - f}, \quad \text{if } |u + f| < |u - f|; \\ m &= \sqrt[3]{u + f}, \quad \text{if } |u + f| \geq |u - f|, \\ n &= \frac{b^2 - 3ac}{9a^2 m}, \quad \text{if } |m| \neq 0; n = 0, \quad \text{if } |m| = 0, \end{aligned}$$

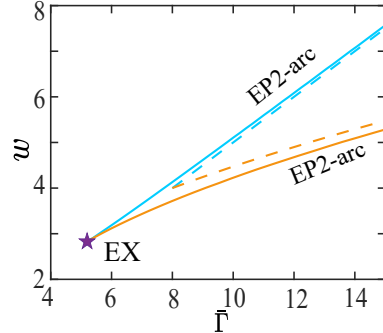


Figure 1. Comparison between the exact results of EAs defined by Eq. (3) (solid curves) and the asymptotic approximations (dashed curves) given by Eqs. (2) and (3) of the main text. The purple pentagram denotes the EX.

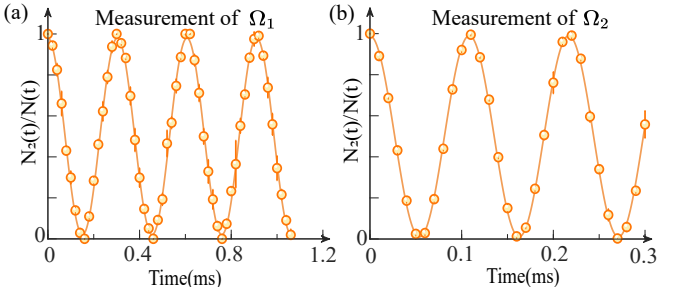


Figure 2. Rabi oscillation measurement for the determination of  $\Omega_1$  in (a) and  $\Omega_2$  in (b). In (a), only the radio-frequency (RF) field that couples  $|F = 1, m_F = -1\rangle$  and  $|F = 1, m_F = 0\rangle$  is turned on, while other fields in the setup are off. In (b), only the microwave field (MW) field that couples  $|F = 1, m_F = -1\rangle$  and  $|F = 2, m_F = 0\rangle$  is turned on, while other fields are absent. In both cases, the BEC is initially prepared in  $|F = 1, m_F = -1\rangle$ . The dots with error bars are the average of three measurements. Solid lines are theoretical fits. The Rabi frequency is read off as  $3.29(1)\pi$  kHz in (a) and  $9.22(3)\pi$  kHz in (b).

where we have

$$\begin{aligned} u &= \frac{9abc - 27a^2d - 2b^3}{54a^3}, \\ f &= \frac{\sqrt{3(4ac^3 - b^2c^2 - 18abcd + 27a^2d^2 + 4b^3d)}}{18a^2}. \end{aligned}$$

By substituting the specific expressions of  $a, b, c, d$  for our case, we obtain the solutions of eigenvalues for arbitrary  $\bar{\Gamma}$  and  $w$  that are illustrated in Fig. 1 of the main text.

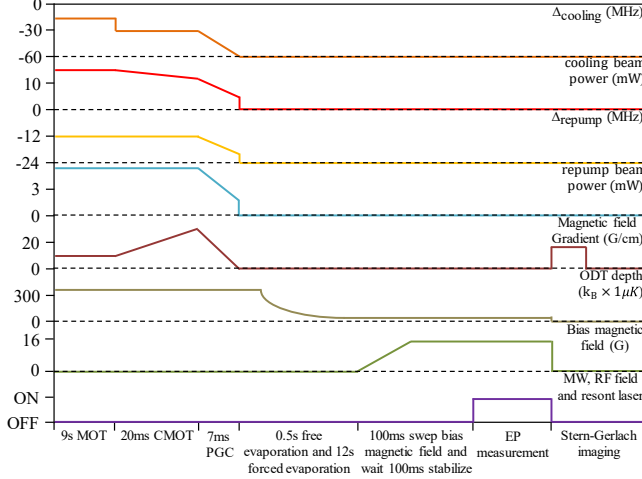


Figure 3. Experimental sequence of creating Rb BEC and inducing relevant dynamics in the main text (that eventually allows us to extract EPs). All axes are not to scale.

## II. EXPERIMENTAL CALIBRATIONS OF THE DISSIPATION RATE AND COUPLING RATES

In this section, we provide details on the experimental calibrations of the dissipation rate  $\Gamma$  and the coupling rate  $\Omega_j$  ( $j = 1, 2$ ) in our setup, respectively.

We first describe in detail the calibration of  $\Gamma$  as shown in Fig. 2(b) of the main text. In our system, a resonant laser is used to drive a transition from  $|F = 2, m_F = 0\rangle$  to an excited state with a short lifetime, which effectively realizes a dissipation rate  $\Gamma$  in the  $|F = 2, m_F = 0\rangle$ . To experimentally measure  $\Gamma$ , we initialize the atoms in the state  $|F = 1, m_F = -1\rangle$ . Then, the atoms are transferred from  $|F = 1, m_F = -1\rangle$  to the state  $|F = 2, m_F = 0\rangle$  by microwave (MW)  $\pi$  pulse. Afterward, the MW field is turned off while the resonant laser is turned on. We measure the time evolution of the atomic population  $N_3$  in the state  $|F = 2, m_F = 0\rangle$ , as shown in the left panel of Fig. 2(b) of the main text. By fitting the data via the empirical formula  $N_3(t) = N_0 e^{-2\Gamma t}$ , we read off the dissipation rate  $\Gamma$ . By measuring  $\Gamma$  under a wide range of laser power  $P_L$  [see right panel of Fig. 2(b) in the main text], we calibrate the relation  $P_L$  and  $\Gamma$  through the fitting via the formula  $\Gamma = AP_L + B$ . This eventually allows to control  $\Gamma$  by controlling the laser power.

To determine  $\Omega_1$  ( $\Omega_2$ ) in Eq. (1) of the main text, we perform the standard measurements of Rabi oscillations of the BEC in the only presence of RF field (MW field) in a two-level configuration, while other driving fields are turned off (i.e.,  $\Gamma = 0$ ); see supplementary Fig. 2(a) and (b). The atom populations at time  $t$  are measured via the usual Stern-Gerlach absorption imaging technique. As illustrated in the supplementary Fig. 2, we extract the Rabi frequencies from standard procedures, thus obtaining  $\Omega_1$  and  $\Omega_2$ , respectively.

To achieve various  $w$  in Figs. 2 and 3 in the main text, we use the following parameters in our experiments: For  $w = 4.5$ , we use  $\Omega_1 = 6.98$  kHz and  $\Omega_2 = 31.41$  kHz; for

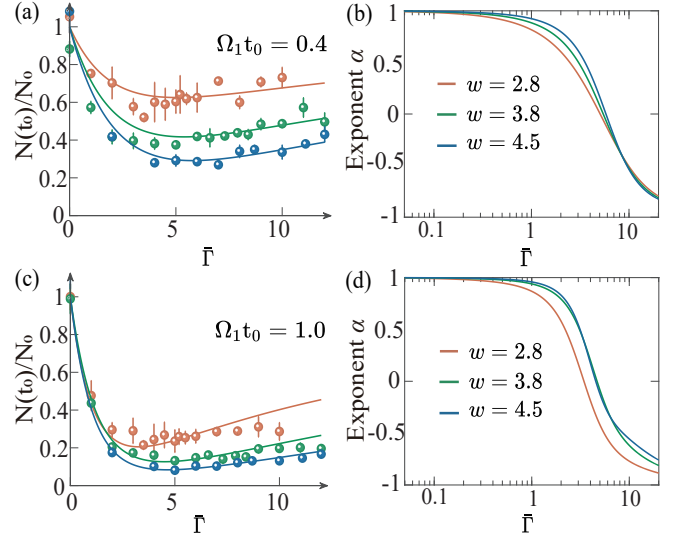


Figure 4. Measured atom number  $N(t_0)/N_0$  (normalized to the initial number  $N_0$ ) at (dimensionless) time (a)-(b)  $\Omega_1 t_0 = 0.4$  and (c)-(d)  $\Omega_1 t_0 = 1$  as a function of the dissipation rate  $\bar{\Gamma}$ . In (a) and (c), the experimental data for the coupling rate  $w = 2.8, 3.8, 4.5$  are depicted by brown, green, and blue dots, respectively. All data within  $\Omega_1 t_0 = 0.4 \pm 0.05$  are shown in (a), and the data within  $\Omega_1 t_0 = 1 \pm 0.05$  are shown in (c). Each data is the mean of three measurements. The error bar denotes the  $1\sigma$  standard deviation. The solid curves are the numerical fittings. (b) and (d): Exponent  $\alpha$  as a function of  $\bar{\Gamma}$  for (b)  $\Omega_1 t_0 = 0.4$  and (d)  $\Omega_1 t_0 = 1$ . Assuming the fitted  $N(t_0)/N_0$  in (a) and (c) is of the form  $N(t_0)/N_0 = \exp(-\gamma t_0)$  with the scaling  $\gamma \propto \bar{\Gamma}^\alpha$ , we extract the exponent  $\alpha$  as a function of  $\bar{\Gamma}$ , for  $w = 2.8, 3.8, 4.5$  (brown, green, and blue), respectively. Other parameters are the same as Fig. 3 (a) of the main text.

$w = 4.2$ , we use  $\Omega_1 = 7.48$  kHz and  $\Omega_2 = 31.41$  kHz; for  $w = 3.8$ , we use  $\Omega_1 = 8.267$  kHz and  $\Omega_2 = 31.41$  kHz; for  $w = 3$ , we use  $\Omega_1 = 10.47$  kHz and  $\Omega_2 = 31.41$  kHz; for  $w = 2.8$ , we use  $\Omega_1 = 10.36$  kHz and  $\Omega_2 = 29.008$  kHz.

## III. SUPPLEMENTARY DATA ON SYSTEM DYNAMICS

Here, we provide additional materials on the system dynamics to supplement the experiment data and analysis in the main text.

In supplementary Fig. 3, we show the typical experimental sequence including creating the BEC and inducing the system dynamics that eventually allow us to extract EPs. Specifically, each experimental sequence starts with a BEC at the state  $|F = 1, m_F = -1\rangle$ . After obtaining BEC, the bias magnetic field is swept to 16 G within 100 ms and waits for 100 ms to stabilize. Next, we turn on the MW field, RF field, and resonant laser simultaneously. A Stern-Gerlach separation followed by absorption imaging is used to measure the atom number of different spin states after a 10 ms time of flight.

In Fig. 3(a) of the main text, we present  $N(t_0)/N_0$

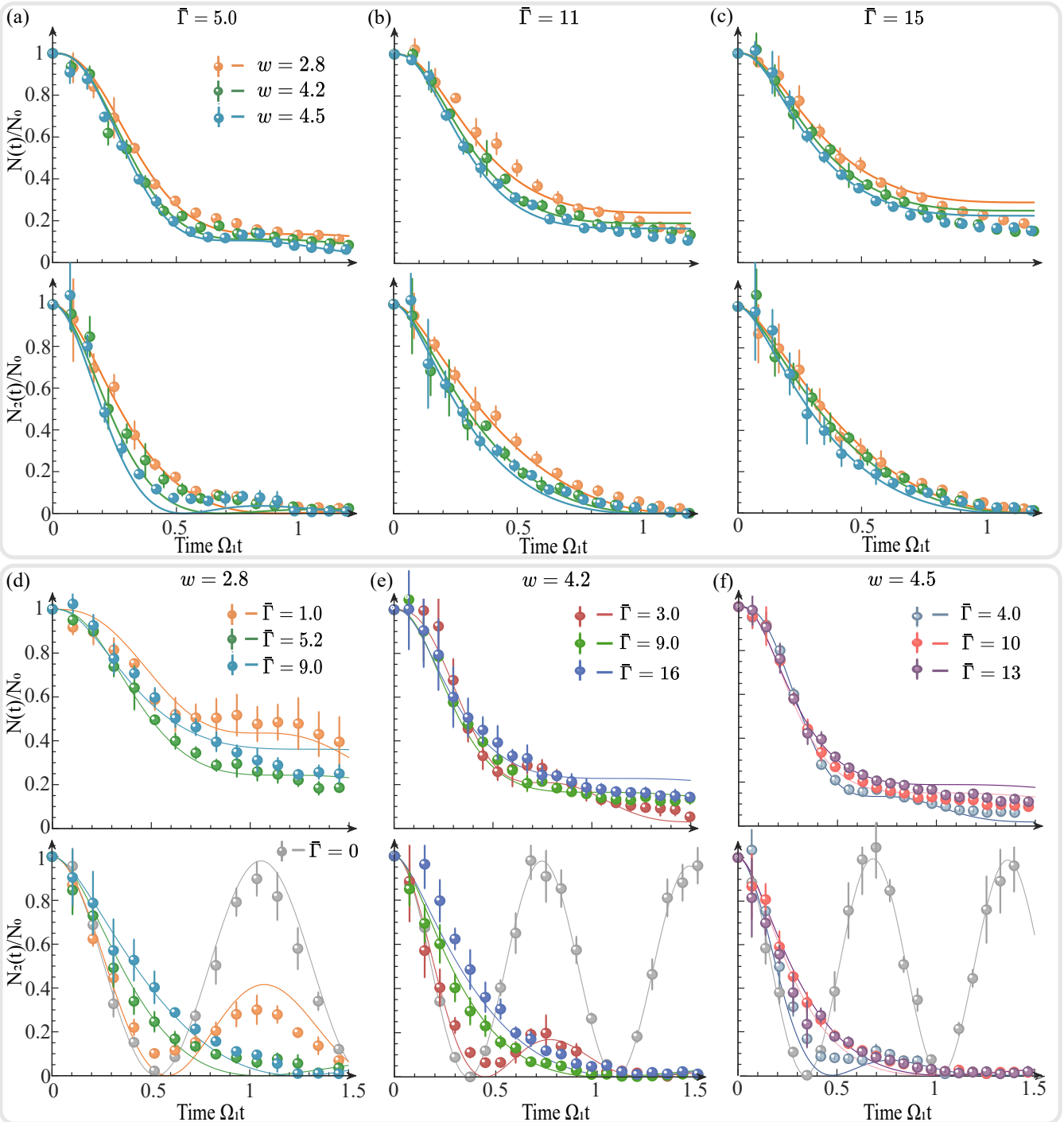


Figure 5. Measured total atom number  $N(t)/N_0$  and the corresponding  $N_2(t)/N_0$  in the state  $|F = 1, m_F = -1\rangle$  as a function of time, for various  $w$  and  $\bar{\Gamma}$ . In the top block, we compare the cases  $\bar{\Gamma} \sim w$ ,  $\bar{\Gamma} > w$  and  $\bar{\Gamma} \gg w$ . In the bottom block, for each  $w$ , we compare the cases  $w > \bar{\Gamma}$ ,  $w \sim \bar{\Gamma}$  and  $w < \bar{\Gamma}$ . Each data is the average value from three measurements. The error bar denotes the  $1\sigma$  standard error. The solid curves are the numerical fittings.

for  $\Omega_1 t_0 = 0.8 \pm 0.05$ . For the purpose of generality, we provide more data on different  $t_0$ , as shown in supplementary Fig. 4. Whatever  $t_0$ , we see that the behaviors of  $N(t_0)/N_0$  [Figs. 4(a) and (c)] share similar features as that in Fig. 3(a) of the main text. Namely, in the strong coupling regime  $\bar{\Gamma} \lesssim w$ , the curves under vari-

ous  $w$  significantly overlap indicating insensitivity of the loss rate to  $w$ ; whereas, in the strong dissipation regime  $\bar{\Gamma} \gg w$ , there is clear difference of  $N(t_0)/N_0$  for various  $w$ , in accordance with the analysis in the quantum Zeno (QZ) regime. Furthermore, as shown in Fig. 4(b) and (d), when increasing  $\bar{\Gamma}$ , the scaling behaviors  $\gamma \sim \bar{\Gamma}^\alpha$

crossover from  $\gamma \propto \bar{\Gamma}$  and tend toward  $\gamma \propto \bar{\Gamma}^{-1}$ .

In supplementary Fig. 5, we show more data on the measured  $N(t)/N_0$  and the corresponding  $N_2(t)/N_0$  under various  $\bar{\Gamma}$  and  $w$ . In Figs. 5(a)-(c), we compare the behaviors of total atom number  $N(t)/N_0$  and the corresponding atom number  $N_2(t)/N_0$  in  $|F = 1, m_F = -1\rangle$  under various  $w$ , when  $\bar{\Gamma} = 5, 10, 15$ , respectively, corresponding to  $\bar{\Gamma} \sim w$ ,  $\bar{\Gamma} > w$  and  $\bar{\Gamma} \gg w$ . We first analyze the behavior of total atom number  $N(t)/N_0$ . For a given  $\bar{\Gamma}$ , we see that the smaller  $w$  always leads to smaller atom loss. This is expected, as the atoms initialized in  $|F = 1, m_F = -1\rangle$  can only escape the system via transiting to the state  $|F = 2, m_F = 0\rangle$ , and, therefore, the smaller is the transition rate  $w$ , the smaller the total loss is, as mentioned in the main text. Moreover, we see that the atom loss is clearly suppressed for very strong dissipation  $\bar{\Gamma}$  compared to  $w$ , as expected from the Zeno effect. Turning to the behavior of  $N_2(t)/N_0$ , we see that for  $\bar{\Gamma} = 5$  comparable to the coupling rate  $w$ , the  $N_2(t)/N_0$  undergoes faster oscillation with larger  $w$ , indicated by smaller  $t_m$  when  $N_2(t)/N_0 \sim 0$  first occurs, in agreement with the behavior of  $\text{Re}(E_j)$  in this regime. In Figs. 5(d)-(f), we consider  $w = 2.8, 4.2, 4.5$ ; for each  $w$ , we compare total atom number  $N(t)/N_0$  and the corresponding atom number  $N_2(t)/N_0$  for  $w > \bar{\Gamma}$ ,  $w \sim \bar{\Gamma}$  and  $w < \bar{\Gamma}$ , respectively. Similar behaviors as Figs. 5(a)-(c) are found.

#### IV. FITTING METHOD

In this section, we provide details on the fitting methods used in Fig. 2 and Fig. 3 in the main text.

For the measured dynamics of atom number in Fig. 2 and Fig. 3, we fit as follows. For example, for the experimental data of total atom number  $N(t)/N_0$ , we fit it by fitting the Hamiltonian parameters  $\bar{\Gamma}$  and  $w$ , respectively. In the fitting process, the system parameters are iteratively improved until the difference of the calculated time evolution of  $N(t)/N_0$  according to the fitted Hamiltonian  $H$  and the measured data are minimized in the least-square sense. Then, by diagonalizing  $H$  with the fitted parameters, we obtain the data of corresponding eigenvalues that are illustrated in Figs. 3(d)-(g) in the main text.

We turn to describe the identification of EPs by fitting. In Figs. 3(d)-(g) of the main text, we fit the experimental eigenvalues as a function of  $\bar{\Gamma}$  through two approaches. In the first approach, we use the expression of eigenvalues with  $w$  as the fitting parameters. In the second approach, we use the empirical expression  $\text{Re}(E_1)/\Omega_1 = A(\Gamma_1 - \bar{\Gamma})^{s_1}[1 - \Theta(\bar{\Gamma} - \Gamma_1)] + B(\bar{\Gamma} - \Gamma_2)^{s_2}\Theta(\bar{\Gamma} - \Gamma_2)$  to fit the experimental data of the real parts of the eigenvalues, where  $\Theta(x)$  is the step function. The EP2s identified from the two approaches agree well with each other. In the main text, the fitting curve is from the first approach, which is also applicable to the imaginary parts.

#### V. THEORETICAL ANALYSIS ON THE PERTURBATION BEHAVIOR AROUND EX

Here we follow Refs. [1, 2] and present detailed theoretical descriptions of the perturbation properties around the EX in the main text. We will discuss different aspects including the anisotropic eigenvalue scalings, phase rigidity, and the braiding property, as summarized in Fig. 6.

At the EX (EP3), the Hamiltonian  $H$  is defective: there exists degenerate eigenvalue  $E_0$  and one independent eigenstate denoted by  $\psi_0$ , i.e.,  $(H - E_0)|\psi_0\rangle = 0$ ; Moreover, the  $\psi_0$  with  $|\psi_1\rangle, |\psi_2\rangle$  form the Jordan chain, i.e.,  $(H - E_0)|\psi_m\rangle = |\psi_{m-1}\rangle$  ( $m = 1, 2$ ). Now suppose the system is subjected to a perturbation  $H_1$ , and the perturbed Hamiltonian is denoted as  $H' = H + zH_1$ , where  $z \in \mathbb{C}$  is the complex perturbation parameter ( $|z|/\Omega_1 \rightarrow 0$ ). The perturbed Hamiltonian can be diagonalized, with three eigenvalues  $E'_j$  and independent eigenstates  $\psi'_j$  ( $j = 1, 2, 3$ ).

We now briefly recapitulate the properties of the perturbed eigenvalues and eigenstates within the perturbation theory of non-Hermitian systems [1]. Depending on the parameter

$$\lambda = \psi_0^T H_1 \psi_0, \quad (4)$$

there are two scenarios.

(1)  $\lambda \neq 0$ . In this case, at the leading order of perturbative expansion, one has

$$\begin{aligned} \delta E_j &\equiv E'_j - E_0 = \lambda^{1/3} z^{1/3}, \\ \delta \psi_j &\equiv \psi'_j - \psi_0 = \lambda^{1/3} \psi_1 z^{1/3}, \end{aligned} \quad (5)$$

for  $j = 1, 2, 3$ . That is, the three perturbed eigenvalues and eigenstates correspond to the three branches of a cube-root expansion. For  $H$  in our case, the perturbation  $H_1 = \Omega_1|3\rangle\langle 3|$  considered in Fig. 4(a) of the main text belongs to this scenario.

(2)  $\lambda = 0$ . In this case, the leading terms for two of the eigenvalues and eigenstates ( $j = 1, 2$ ), respectively, are given by

$$\begin{aligned} \delta E_j &= \pm \lambda_1^{(1)} z^{1/2}, \\ \delta \psi_j &= \lambda_1^{(1)} \psi_1 z^{1/2}, \end{aligned} \quad (6)$$

with  $\lambda_1^{(1)} = (2\psi_1^T H_1 \psi_0)^{1/2}$ . That is, two eigenvalues (eigenstates) correspond to the two branches of a square-root expansion, while the remaining eigenvalue and the eigenstate follow the usual Taylor expansion.

The above anisotropic scaling behavior is related to the hybrid topological property of the EX. This can be revealed by the phase rigidity of the perturbed eigenstate  $\psi'_j$  ( $j = 1, 2, 3$ ), which is defined as [2]

$$r_j = \frac{\left| \langle \psi_j'^L | \psi_j'^R \rangle \right|}{\langle \psi_j'^R | \psi_j'^R \rangle}, \quad (7)$$

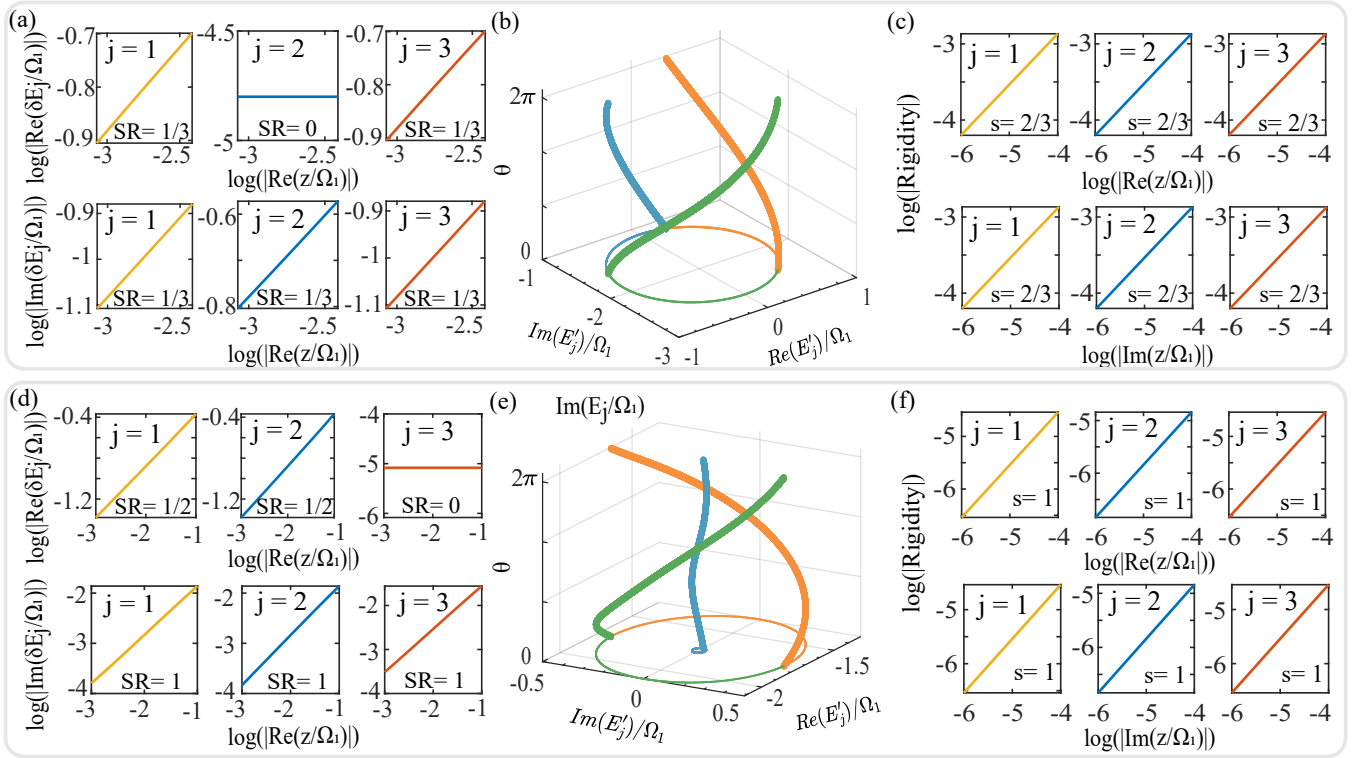


Figure 6. Eigenvalue anisotropy and hybrid topological properties for the EX in the main text. The perturbed Hamiltonian is  $H' = H + zH_1$ , with the complex perturbation parameter  $z/\Omega_1 = 0.1e^{i\theta}$  [ $\theta \in [0, 2\pi]$ ]. (a)-(c):  $z^{1/3}$  behavior, when  $H_1 = |3\rangle\langle 3|$ . (d)-(f):  $z^{1/2}$  behavior, when  $H_1$  is given by Eq. (4) of the main text. In each case, we calculate the eigenvalues and eigenstates of  $H'$ . (a) and (d): Real and imaginary parts of  $\delta E_j/\Omega_1$  ( $j = 1, 2, 3$ ) as a function of  $\text{Re}(z)$  in the log-log plot. The power exponent SR in the leading perturbative expansion term is extracted from the slope. (b) and (e): Braiding diagram formed by the complex eigenvalue bands with  $\theta \in [0, 2\pi]$ . (c) and (f): Phase rigidity and critical exponent  $s$ . Phase rigidity of the perturbed eigenstates is calculated as a function of  $\text{Re}(z/\Omega_1)$  and  $\text{Im}(z/\Omega_1)$  in the log-log plot, respectively. The critical exponent  $s$  is extracted from the slope.

where  $L$  and  $R$  are used to label the left and right eigenstates, respectively. The critical exponent of the phase rigidity is given by

$$s = \frac{\partial \log r_j}{\partial (\log |z|/\Omega_1)}. \quad (8)$$

The scenario (1) is characterized by  $s = 1/3$ , while the scenario (2) is characterized by  $s = 1$ . The  $s = 1$  has a direct correspondence to the winding number 2/3: When the EX is encircled, the perturbed eigenstate picks up a Berry phase  $2\pi$  after three cycles, leading to the winding number 2/3. The  $s = 1$ , on the other hand, corresponds to when the perturbed eigenstate picks up a Berry phase  $2\pi$  after two cycles, leading to the winding number 1. The hybrid nature of topological property can also be visualized from the so-called braiding diagram [3-7].

In Figs. 6(a)-(c), we consider the perturbed Hamiltonian  $H' = H + z|3\rangle\langle 3|$  as Fig. 4(a) of the main text. We take  $z/\Omega_1 = 0.1e^{i\theta}$  [ $\theta \in [0, 2\pi]$ ] in our calculations. In Fig. 6(a), we calculate the corresponding perturbed eigenvalues and show the real and imaginary parts of  $\delta E_j$  ( $j = 1, 2, 3$ ) as a function of  $\text{Re}(z/\Omega_1)$  in the log-log plot. From it, we extract the power exponent  $\text{SR} = 1/3$ , i.e.,

the cubit-root scaling  $z^{1/3}$  characteristic of scenario (1). Moreover, we numerically track the eigenvalues of  $H'$  in the complex  $z$  plane and show the braiding diagram in Fig. 6(b). There, we see three complex-energy bands (denoted by strands with different colors) braid around each other after a  $2\pi$  variation of  $\theta$ . In Fig. 6(c), we calculate the phase rigidity  $r_j$  for each eigenstate and show it as a function of  $\text{Re}(z/\Omega_1)$  and  $\text{Im}(z/\Omega_1)$  in the log-log plot, respectively. We see that for all eigenstates, the critical exponent is  $s = 2/3$ .

In Figs. 6(d)-(f), we consider  $H' = H + zH_1$ , where  $H_1$  is given by Eq. (4) of the main text. In Fig. 6(d), we find  $\text{SR} = 1/2$  for the real parts of two eigenvalues, i.e., the square-root scaling  $z^{1/2}$  characteristic of scenario (2). Note the corresponding imaginary parts scale as  $\propto z$  at the leading order, meaning the leading correction of two eigenvalues is purely real. The third perturbed eigenvalue is purely imaginary, and the leading correction is linear in  $z$  (i.e., in Taylor expansion). The corresponding braiding diagram is shown in Fig. 6(e). There, we see that only two bands braid around each other. This is consistent with Fig. 6(f), which shows the critical exponent of the phase rigidity of the perturbed eigenstate is  $s = 1$ .

---

<sup>\*</sup> These two authors contributed equally.

<sup>†</sup> huying@sxu.edu.cn

<sup>‡</sup> zhaoyt@sxu.edu.cn

- [1] G. Demange and E.-M. Graefe, Signatures of Three Coalescing Eigenfunctions, *J. Phys. A: Math. Theor.* **45**, 025303 (2012).
- [2] Y.-X. Xiao, Z.-Q. Zhang, Z. H. Hang, and C. T. Chan, Anisotropic Exceptional Points of Arbitrary Order, *Phys. Rev. B* **99**, 241403(R) (2019).
- [3] K. Wang, A. Dutt, C. C. Wojcik, and S. Fan, Topological Complex-Energy Braiding of Non-Hermitian Bands, *Nature* **598**, 59 (2021).
- [4] H. Hu and E. Zhao, Knots and Non-Hermitian Bloch Bands, *Phys. Rev. Lett.* **126**, 010401 (2021).
- [5] Y. S. S. Patil, J. Höller, P. A. Henry, C. Guria, Y. Zhang, L. Jiang, N. Kralj, N. Read, and J. G. E. Harris, Measuring the Knot of Non-Hermitian Degeneracies and Non-Commuting Braids, *Nature* **607**, 271 (2022).
- [6] H. Hu, S. Sun, and S. Chen, Knot Topology of Exceptional Point and Non-Hermitian No-Go Theorem, *Phys. Rev. Res.* **4**, L022064 (2022).
- [7] C. X. Guo, S. Chen, K. Ding, and H. Hu, Exceptional Non-Abelian Topology in Multiband Non-Hermitian Systems, *Phys. Rev. Lett.* **130**, 157201 (2023).